Hindawi
International Journal of Aerospace Engineering
Volume 2023, Article ID 7843757, 20 pages
https://doi.org/10.1155/2023/7843757

Research Article

Aerodynamic Load Reduction on a Supercritical Airfoil Using Tilted Microjets

Cheng Xue,[1] **Feng Deng**,[1] **Haifeng Wang**,[1] **and Ning Qin**[2]

[1]*Nanjing University of Aeronautics and Astronautics, Nanjing 210016, China*
[2]*The University of Sheffield, Sheffield, S1 3JD, UK*

Correspondence should be addressed to Feng Deng; fdeng@nuaa.edu.cn

Received 21 October 2022; Revised 15 January 2023; Accepted 31 January 2023; Published 18 February 2023

Academic Editor: Alex Zanotti

Microjets arranged on the wing surfaces of civil transport aircraft have been shown to have great potential in suppressing high-frequency gust loads. This paper presents a study of aerodynamic load reduction on a supercritical airfoil using tilted microjets by solving the Reynolds-averaged Navier-Stokes (RANS) equations. The numerical method was first validated against the experimental and previous numerical data. Afterward, the subsonic and transonic flowfields around the supercritical airfoil were simulated with various angled microjets. The results show that both the lift reduction and the power efficiencies significantly increase as the blowing direction shifts downstream to upstream. The movement and weakening of the shock due to the jet are observed at $\alpha > 2^{\circ}$ in transonic flow, resulting in a drag reduction compared to the baseline airfoil. However, the transient subsonic results revealed that the upstream jet induces a strong vortex shedding, which is suppressed in transonic flows. During jet deployment, there are three distinct phases: time lag, vortex rolling-up, and rebalancing, in that order. Once it reaches the trailing edge in subsonic flows, the starting vortex rapidly modifies the load and induced a strong roll-up vortex from the pressure surface. Nevertheless, in transonic flow, the rebalancing stage contributes to a greater reduction in lift due to the additional shock movement and weakening effect.

1. Introduction

Gust loads have a huge impact on the designs of civil transport aircraft [1]. Relieving the impacts of the gust loads can bring the benefits of lowering the structural weight of an aircraft [2] and improving passenger comfort, which will greatly increase its competitiveness. Traditionally, control systems using moving surfaces [3, 4] are adopted to optimize the load distribution during gust encounters and maneuvers. These systems often utilize the existing control surfaces, such as ailerons, flaps, and spoilers. However, these actuators are initially designed for aircraft maneuvering and have relatively high inertia. Generally, the effective response frequency of flaps and ailerons is often lower than 10 Hz, and the gust loads with higher frequency have to be borne by the aircraft structure at the cost of increased structure weight.

In recent years, mechanical or fluidic microactuators have been developed to suppress the gust loads that traditional devices cannot cope with. Microactuators have been investigated for flow control for many years. For example, they were used to delay transitions [5], prevent separations [6], or increase lift [7, 8]. More recently, some studies have

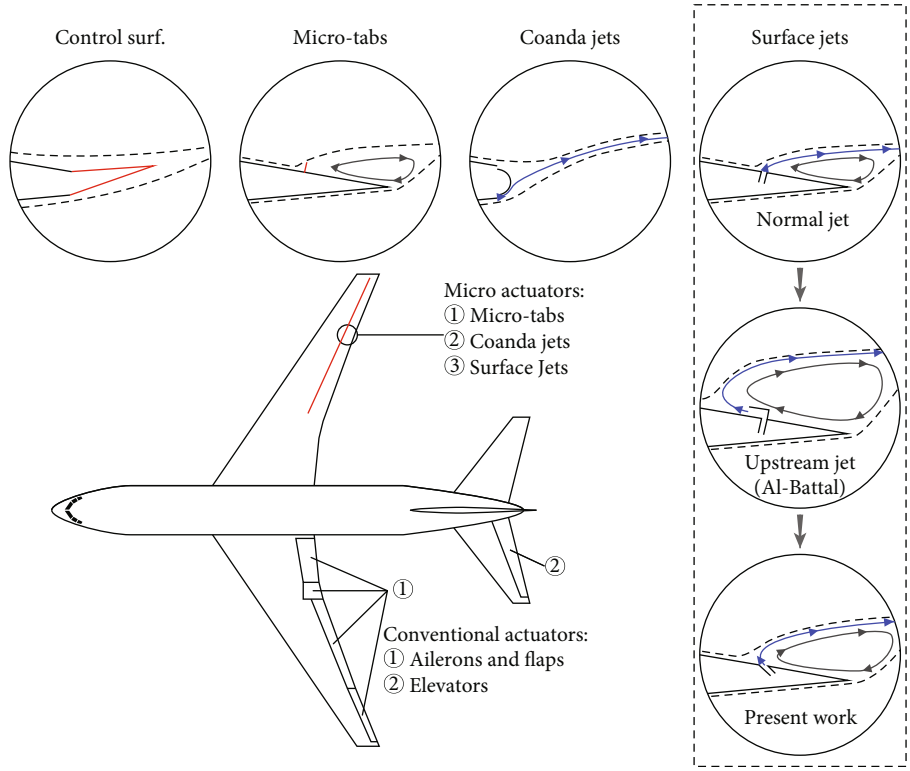

Figure 1: The illustration of various load control methods.

explored the possibility of applying microactuators in aerodynamic load control. For example, microtables [9], microjets [10, 11], and Coanda jets [12] have been proven to be able to reduce the airfoil lift effectively in steady actuation. Figure 1 illustrates the main types of actuators on a typical civil transport aircraft for aerodynamic load control, including the conventional control surfaces, the mechanical microtabs, and the fluidic actuators.

Although the mechanical microtabs can achieve a high-frequency response, deploying spanwise-distributed microtabs requires the cooperation of multiple mechanical structures, reducing the system's reliability. Also, the lift change produced by the microtab is not directly proportional to the tab height, which complicates the design of the control system [13]. On the other hand, the fluid actuators are relatively simpler, requiring only a few valves to control. Furthermore, the lift reduction by the fluid actuators was found to be approximately linear, with the square root of the momentum coefficient defined as $C_\mu = \dot{m}U_j/((1/2)\rho_\infty U_\infty^2 c)$ [10–12, 14–18], where $\dot{m}$ is the jet mass flow rate, U_j is the jet velocity magnitude, $(1/2)\rho_\infty U_\infty^2$ is the freestream dynamic pressure, and c is the chord length. Therefore, it can be approximated as $\Delta C_L \propto \sqrt{C_\mu} \propto U_j$ at low Mach numbers. This relation is also consistent with the theoretical results for the thin airfoil with jet flaps [19]. This can facilitate the better design of the control system.

Khalil et al. [20] numerically compared the efficiency of various load control actuators. They found that the lift and pitching moment responses of fluidic actuators were similar to the conventional flaps, while the drag penalty of these fluidic actuators was generally smaller than that of the mechanical ones. Notably, compared with normal jets, Coanda jets require a smaller momentum coefficient for the same lift reduction. However, using Coanda jets usually results in a thick rounded trailing edge, which will increase aircraft drag at cruise conditions [18]. In addition, Coanda jet holes are typically smaller in comparison with normal jet holes, resulting in higher jet velocities and lower efficiency at transonic speeds [12, 18].

Active aerodynamic load control through surface blowing was advocated and experimentally investigated by Al-Battal et al. [11, 21] at low speeds. They found that the jet perpendicular to the airfoil surface was inefficient and proposed replacing the conventional normal jet with the upstream jet. In their experiments, the normal ejected air is blocked by a thin deflection piece and is forcibly deflected by 90° toward upstream (see Figure 1). The upstream blowing moves the rear stagnation point forward, resulting in a larger recirculation zone, thus changing the effective camber. However, the efficiency of upstream blowing in transonic flows is not yet well understood. Moreover, the control efficiency of differently oriented jets of the same width has not been quantitatively compared. Recently, Li and Qin [22] have successfully neutralized the lift augmentation due to a discrete gust with adaptive normal blowing on the trailing edge of an elastic wing. By tilting the jet upstream, it is possible to improve the energy efficiency of the load control.

Additionally, most previous studies focused on studying the change of lift with a given momentum coefficient. The energy consumption caused by the jet system is still unknown. One of the exceptions is the study conducted by Lefebvre et al. [23]. They investigated the pumping power

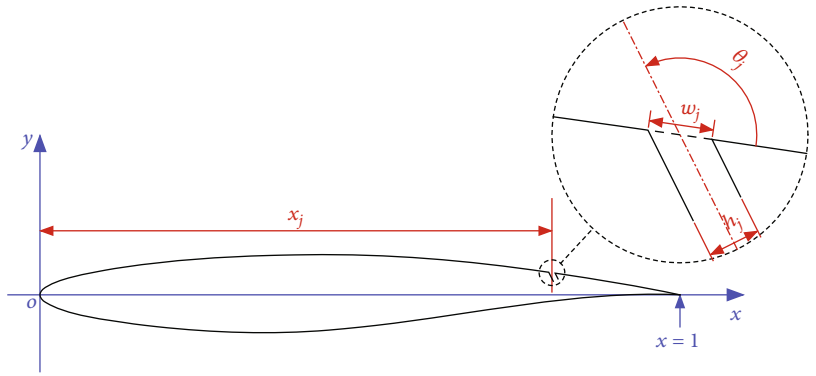

Figure 2: Definition of the jet geometric parameters.

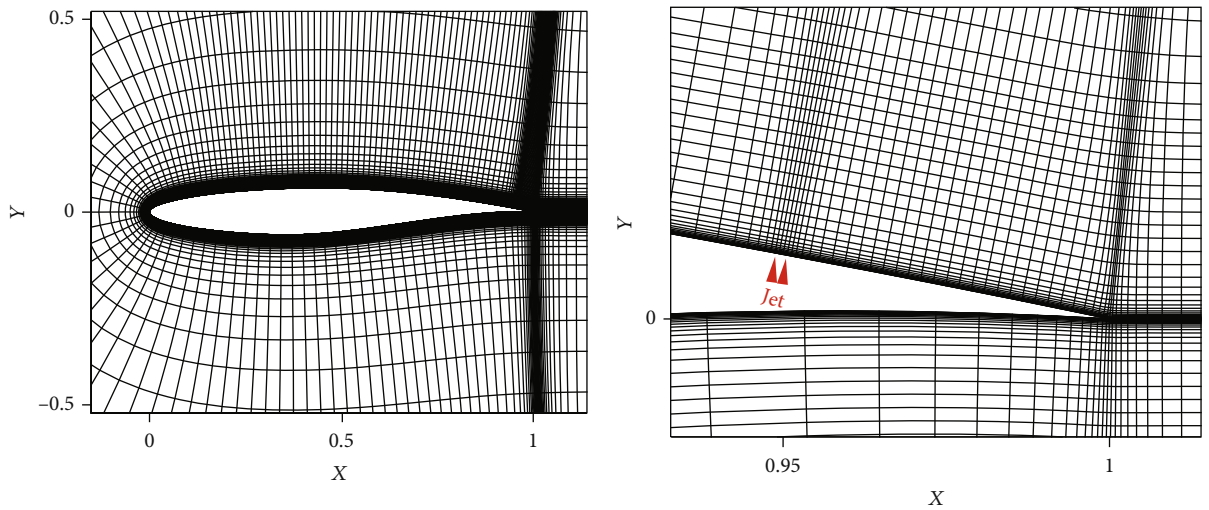

(a) Generated grid

(b) Surface jet boundary

Figure 3: The computational grid around RAE2822 airfoil with a normal jet on the suction surface (every 4 points).

consumption of coflow jets and proposed an expression for measuring airfoil efficiency based on power consumption.

Following the previous works, this paper is aimed at further investigating the influence of jet-blowing direction on load control efficiency and understanding the associated flow physics for a supercritical airfoil in subsonic and transonic flows. The RAE2822 airfoil was chosen for this study because it possesses the essential characteristics of the supercritical airfoils used on modern transport aircraft. Furthermore, researchers are also familiar with its aerodynamic properties. The flowfields around the RAE2822 airfoil equipped with five different oriented jets are numerically simulated by solving for the Reynolds-averaged Navier-Stokes (RANS) equations. The jet system is assumed to be directly fed from the incoming flow and has no energy losses or heat exchange during pumping. The efficiencies measured by both momentum coefficient and energy consumption for different configurations and flow conditions are compared. Unsteady simulations were also carried out to further understand the transient process of jet deployment.

The RANS results show that the dominant power consumption is the drag penalty due to momentum change, and tilting the jet upstream improves the load control effect and energy efficiency. An additional load reduction due to the movement and weakening of normal shock is observed in the transonic cases. Preliminary unsteady simulations of jet deployment are also performed. However, the transient results show that the upstream jet is unable to achieve the RANS results due to the presence of vortex shedding in subsonic flow but meets the expectations in transonic flow. Meanwhile, three stages of the jet deployment process are identified during the jet deployment process.

2. Methods

2.1. Microjet Parameters

2.1.1. Jet Geometry. The normal surface jet can be defined by two geometric parameters, namely, the chordwise position x_j and the slit width h_j. To describe the jets with

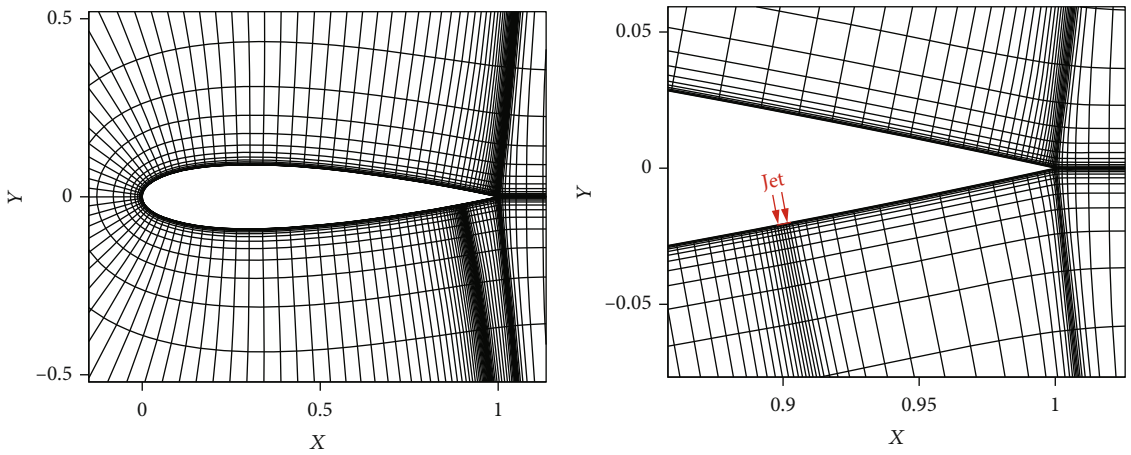

(a) Mesh topology (b) Details in the jet vicinity

Figure 4: Computational grid around the NACA0018 airfoil with normal on the pressure surface(every 4 points).

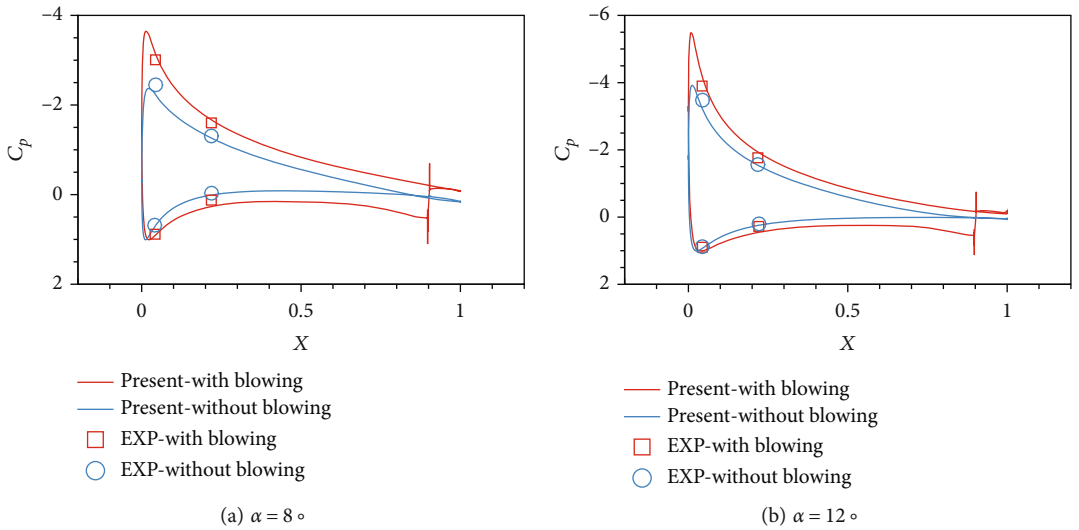

(a) $\alpha = 8^\circ$ (b) $\alpha = 12^\circ$

Figure 5: Pressure coefficient distributions around the NACA0018 airfoil.

different blowing directions, an additional parameter, the jet angle θ_j, is introduced to describe the injection, as shown in Figure 2. $\theta_j = 0^\circ$ defines a jet ejected downstream along the surface, similar to the concept of Coanda jets, while $\theta_j = 90^\circ$ defines a jet perpendicular to the surface, corresponding to the normal jet. According to the definition, the width of the jet exit is derived as $w_j = h_j / \sin\theta_j$. Five steady jets with different blowing angles were chosen for this study, including $\theta_j = 30^\circ$, 60°, 90°, 120°, and 150°. All jets are located at the $x_j = 0.95c$ on the suction side of the RAE2822 airfoil with the same jet width of $h_j = 0.0025c$.

2.1.2. Momentum Coefficient. The jet intensity is usually described using the momentum coefficient C_μ:

$$C_\mu = \frac{\rho_j U_j^2 h_j}{(1/2)\rho_\infty U_\infty^2 c}, \tag{1}$$

where ρ_j is the injection density, U_j is the injection velocity, h_j is the slit width, $(1/2)\rho_\infty U_\infty^2$ is the freestream dynamic pressure, and c is the chord length. In this study, the momentum coefficient is set to $C_\mu = 0.005$ so that the jet velocity magnitude U_j equals the freestream velocity U_∞ in an incompressible flow.

2.1.3. Power Consumption. The jet injection can be achieved by compressing the air with a compressor. According to the analysis by Lefebvre et al. [23], the power consumption can be determined as the following:

$$P_{\text{jet}} = \frac{\dot{m} c_p T_{01}}{\eta} \left(\Gamma^{(\gamma-1)/\gamma} - 1 \right), \tag{2}$$

where $\dot{m}$ is the mass flow rate, T_{01} is the total temperature of jet flow, and $\Gamma = p_{01}/p_{00}$ is the total pressure ratio of the pump. p_{01} is the mass-weighted averaged total pressure of the jet flow. In this study, it is assumed that the pump inlet

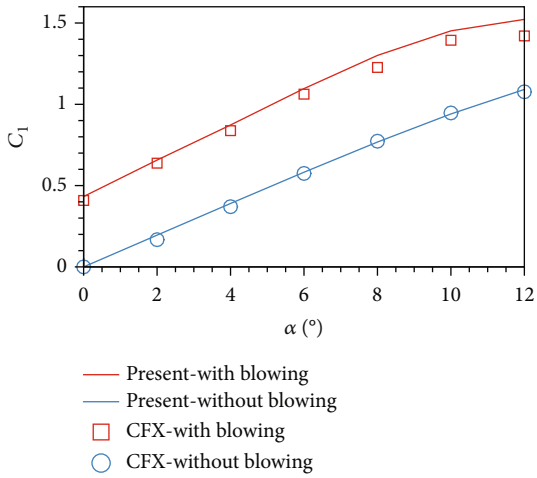

Figure 6: Lift augmentation due to injection on the lower surface of NACA0018 airfoil.

Table 1: RAE 2822 the grid convergence results.

Index	Grid dimension	C_l	C_d
Coarse	489×121	0.6696	0.01257
Medium	673×169	0.6756	0.01233
Fine	965×249	0.6773	0.01224

conditions are the same as freestream total conditions, and the compression is adiabatic. Thus, T_{01} is taken to be the freestream total temperature $T_{0\infty}$ and p_{00} is taken to be the freestream total pressure $p_{0\infty}$. η is the pump efficiency, which is taken to be 1.0 in this study to express the power required to drive the jet. The power consumption can be nondimensionalized with the free-stream dynamic pressure $(1/2)\rho_\infty U_\infty^2$, free-stream velocity magnitude U_∞, and chord length c:

$$C_{\text{power}} = \frac{P_{\text{jet}}}{(1/2)\rho_\infty U_\infty^3 c}. \tag{3}$$

2.2. Mesh Generation. An inhouse code AirfoilMeshers.jl (source code available online: https://github.com/xuecheng/AirfoilMeshers.jl), based on the hyperbolic mesh generation method [24], was used to generate the C-type structured grids for this study. The far-field boundary is extruded $20c$ away from the airfoil surface, and the first layer height near the wall is controlled to maintain the y^+ value to be less than one for near-wall turbulence modeling. The backflow region grids near the trailing edge are approximately square with edge length $\Delta \approx 0.0005c$. The grid space on the suction surface is also refined to $\Delta x \approx 0.0035c$ to capture the movement of normal shock.

Figure 3 shows the generated grid around the RAE 2822 airfoil equipped with a normal microjet ($\theta_j = 90°$). The grid contains a total of 965×249 points, with 217 points on the pressure surface, 445 points on the suction surface, and an extra 17 points across the jet boundary. The number of jet boundary points increases to 21 and 33 for $\theta_j = 60°$ and $\theta_j = 30°$, respectively.

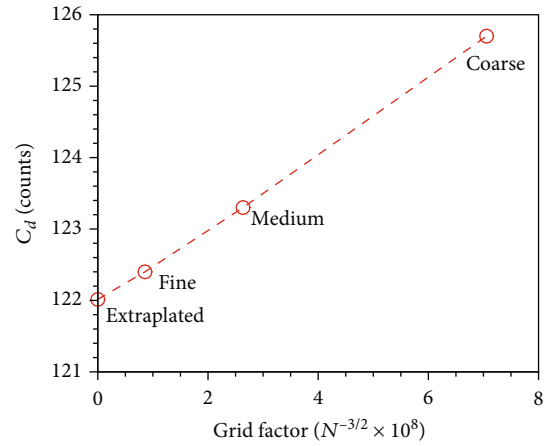

Figure 7: Drag convergence for the RAE2822 airfoil.

2.3. Numerical Methods. The flows around the airfoil with microjets have been simulated via the open-source CFL3D code [25]. CFL3D solves the compressible Reynolds-averaged Navier-Stokes equations on multiblock structured grids. The vector form of the two-dimensional compressible Navier-Stokes equation is

$$\frac{\partial \mathbf{Q}}{\partial t} + \frac{\partial(\mathbf{F} - \mathbf{F}_v)}{\partial x} + \frac{\partial(\mathbf{G} - \mathbf{G}_v)}{\partial y} = 0, \tag{4}$$

where $\mathbf{Q} = [\rho, \rho u, \rho v, E]^T$ is the vector of conserved variables, consisting of the density, momentum, and total energy per unit volume. $\mathbf{F}$ and $\mathbf{G}$ are the convective flux terms. $\mathbf{F}_v$ and $\mathbf{G}_v$ are the viscous flux terms. The third-order upwind-biased MUSCL [26] scheme is chosen for the convective terms, and the second-order central differencing scheme is chosen for the viscous terms. Roe's flux difference-splitting method [27] is used to obtain the fluxes at the cell faces. Turbulence is modeled using Menter's SST two-equation model [28] with curvature correction [29].

To simulate the jet flow, Blaylock et al. [30] have compared three jet models, including a resolved plenum, a uniform velocity inlet, and a velocity inlet with a parabolic profile. Their study shows that the differences among these models are negligible. The velocity inlet method with prescribed density and velocity is enough for incompressible flows. However, the density of jet flow is hard to determine for transonic flows. Lefebvre et al. [23] achieved the specified C_μ by fixing the total temperature and adjusting the total pressure in the injection cavity. This paper adopts a tightly coupled boundary treatment method based on previous works to improve computational efficiency. The boundary condition procedure reads the total temperature T_{0j}, jet momentum $\mu = \rho_j U_j^2$, and jet angle θ_j from the input file. Then, the primitive variables on each boundary face can be calculated by following steps (source code available online:

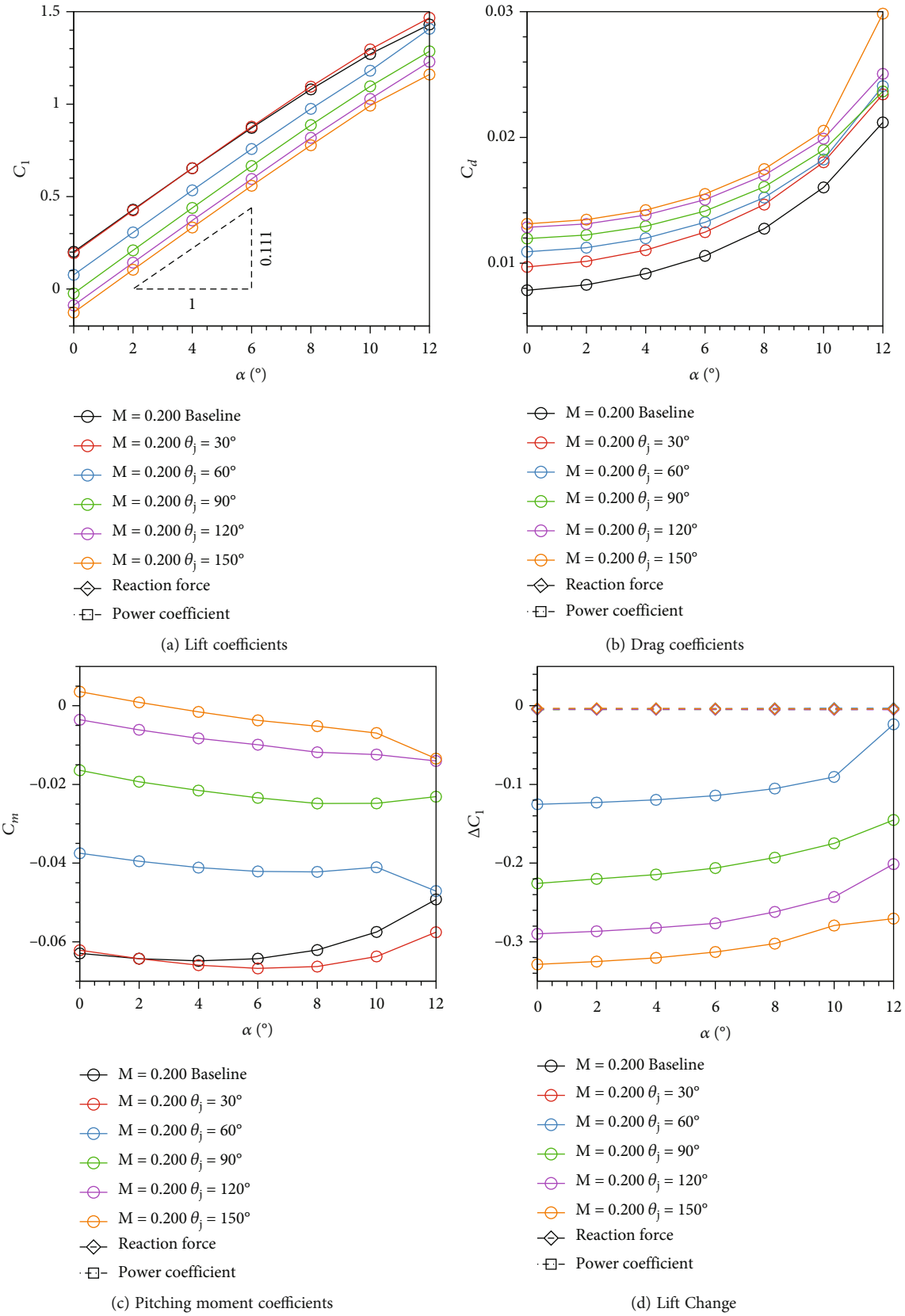

Figure 8: Continued.

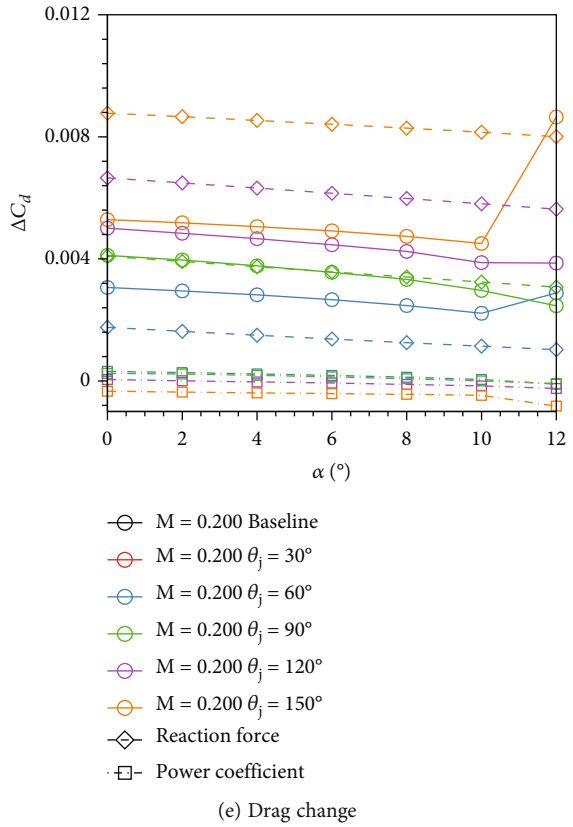

(e) Drag change

Figure 8: Subsonic aerodynamic performances at $M_\infty = 0.2$ and $C_\mu = 0.005$.

https://github.com/xue-cheng/CFL3D/blob/master/source/cfl3d/libs/bc2036.F90):

(1) Linearly extrapolate pressure p_j from adjacent two cells

(2) Take an initial guess of density ρ_j from the adjacent cell

(3) Calculate the velocity magnitude $U_j = \sqrt{\mu/\rho_j}$

(4) Calculate the local sound speed $a_j = \sqrt{\gamma p_j/\rho_j}$ and local Mach number $M_j = U_j/a_j$

(5) Calculate the static temperature $T_j = T_{0j}/(1 + ((\gamma - 1)/2)M_j^2)$

(6) Update local density with the ideal gas law $\rho_j = p_j/(RT_j)$

(7) Repeat steps 3-6 one or more times to correct primitive variables

2.4. Force Calculation. The lift, drag, and pitching moment are automatically integrated along the wall and jet boundaries during the solving process. However, the reaction force caused by the change in jet momentum also needs to be included. This reaction force $\vec{r}$ can be calculated by

$$\vec{r} = -\dot{m}\left(\vec{u}_j - \vec{u}_\infty\right), \tag{5}$$

where $\dot{m}$ is the jet mass flow rate, $\vec{u}_j$ is the jet velocity vector, and $\vec{u}_\infty$ is the freestream velocity vector. The reaction force acting at the jet center is added to the lift, drag, and pitching moment. Finally, the aerodynamic coefficients of the airfoil can be calculated and corrected by the following equations:

$$\begin{aligned} C_l &= \frac{L_a + L_r}{(1/2)\rho_\infty U_\infty^2 c}, \\ C_d &= \frac{D_a + D_r}{(1/2)\rho_\infty U_\infty^2 c} + \max\left(0, C_{\text{power}}\right), \\ C_m &= \frac{M_a + M_r}{(1/2)\rho_\infty U_\infty^2 c^2}, \end{aligned} \tag{6}$$

where L, D, and M are the lift, drag, and pitching moment, respectively. Subscript 'a' indicates the value obtained with surface integration, while subscript 'r' indicates the contribution of the reaction force. The additional power consumption required by the pumping system is added to the drag coefficient by means of the power coefficient.

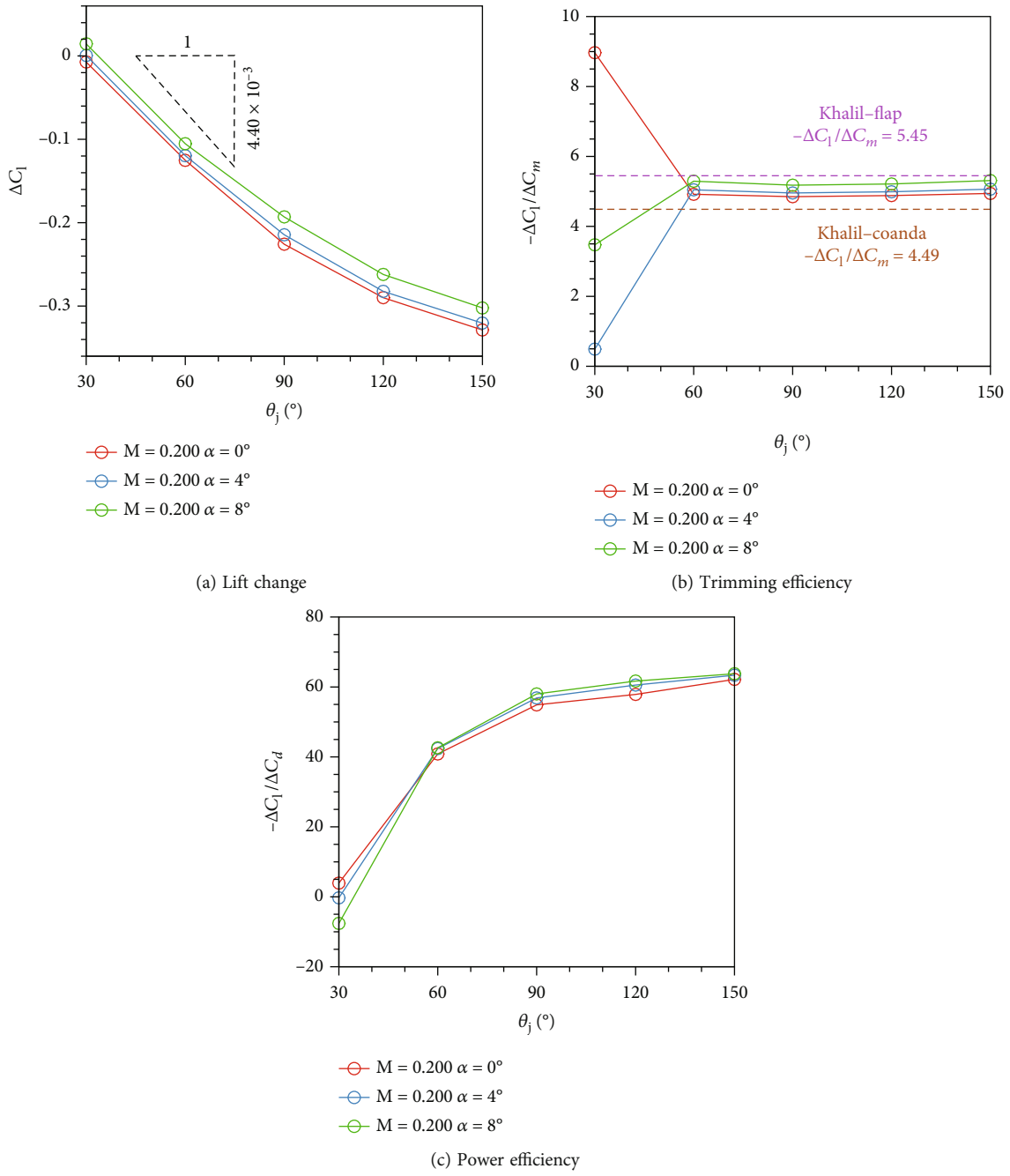

Figure 9: Subsonic control efficiencies with steady blowing at $M_\infty = 0.2$ and $C_\mu = 0.005$.

2.5. Validation. In principle, the microjets for load control are similar to jet flaps for lift augmentation. The main difference is that the jet flap is located on the pressure side while the load control jet is on the suction side. The experimental and computational data on fluidic lift augmentation by de Vries et al. [31] were used to validate the numerical method of this study. The experimental model was a NACA0018 airfoil with a chord length of 0.165 m. The free-stream Mach number and Reynolds number based on the chord length are $M_\infty = 0.176$ and $\mathrm{Re}_c = 6.6 \times 10^5$, respectively. A slit of 0.001 m in width is located with its center at the $x/c = 0.9$. Hot wire anemometry measurements [31] showed the presence of a vena contracta in the slits due to the sharp inner edges within the compartments, and the measured jet velocity is $U_j/U_\infty = 1.2$. Therefore, in the numerical simulations, the slit width has been reduced to 70% of the actual slit width such that the injected momentum is equal to that obtained in the experiments, which is consistent with the numerical model reported in Ref. [31].

The grid around NACA0018 is generated by the methods described in Section 2.2 and plotted in Figure 4. There are a total of 757×101 points, 305 points on the

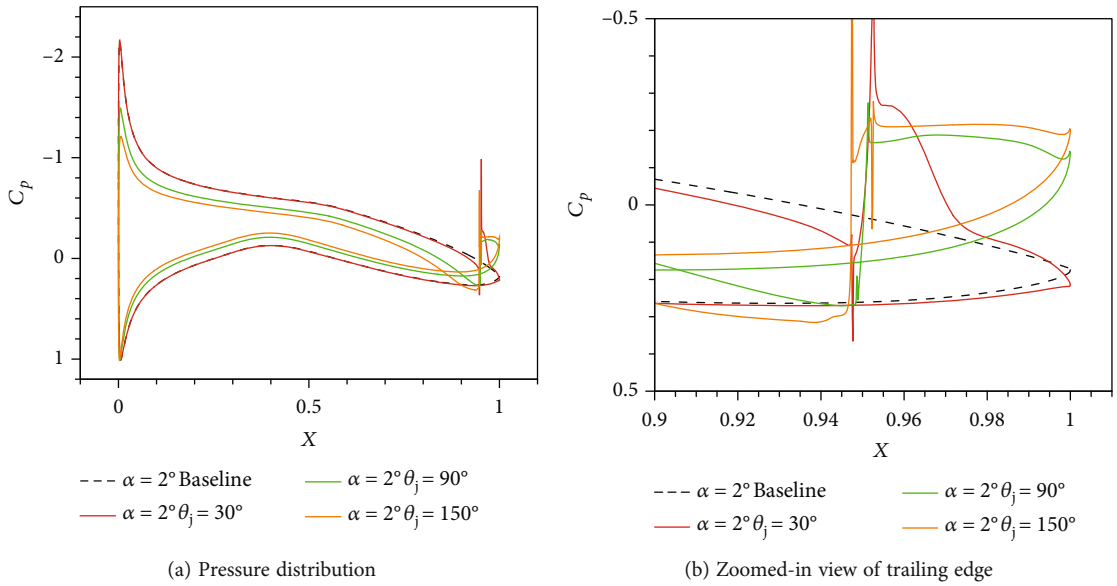

(a) Pressure distribution

(b) Zoomed-in view of trailing edge

Figure 10: Pressure coefficient distributions around the RAE2822 airfoil at $M_\infty = 0.2$, $\alpha = 4\circ$, and $C_\mu = 0.005$.

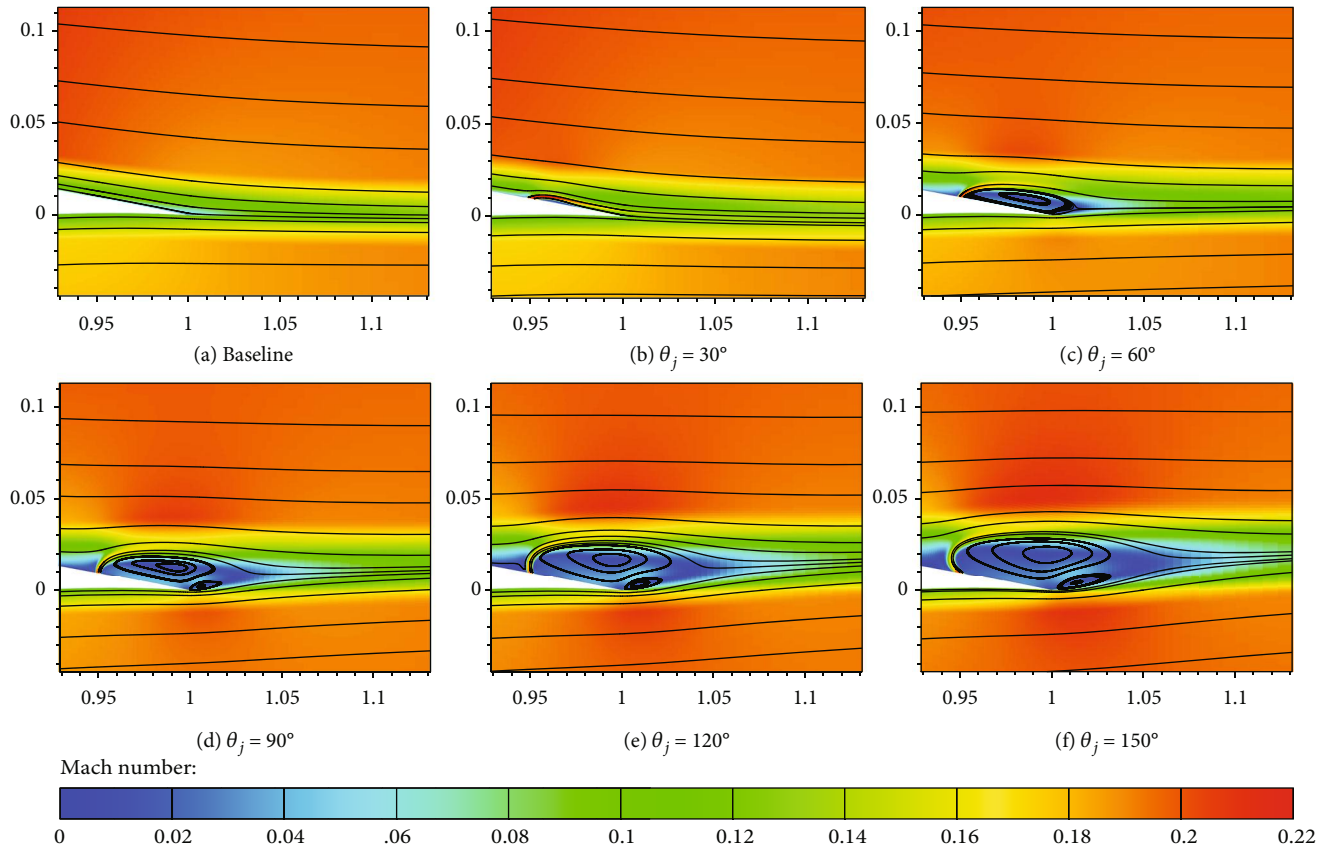

Figure 11: Trailing edge flowfields for different jets at $M_\infty = 0.2$, $\alpha = 4^\circ$, and $C_\mu = 0.005$.

pressure surface, 261 points on the suction surface, and 101 points normal to the wall. The number of cells around the NACA0018 airfoil is fewer than that of the RAE2822 airfoil. This is due to the lower Reynolds number and the absence of normal shocks in the flow field. Figure 5 compares the calculated surface pressure coefficients with and without jets, as well as the experimental data from Ref. [31]. It can be seen that the numerical results show a good agreement with the experimental data. The lift curves are also compared to the numerical results from Ref. [31]. As seen in Figure 6, the lift coefficients calculated by the present method are also in good agreement with the ANSYS CFX results [31].

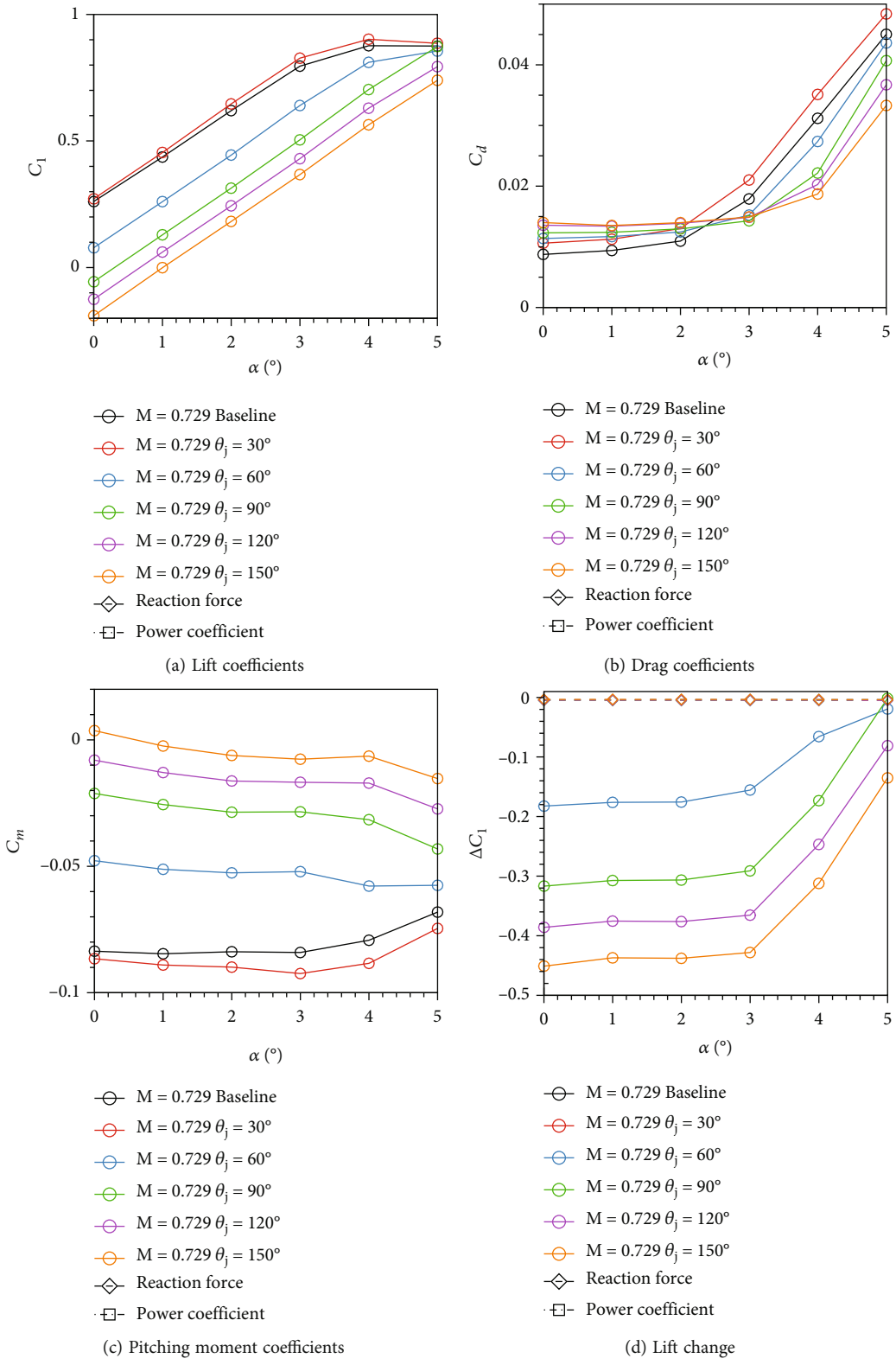

Figure 12: Continued.

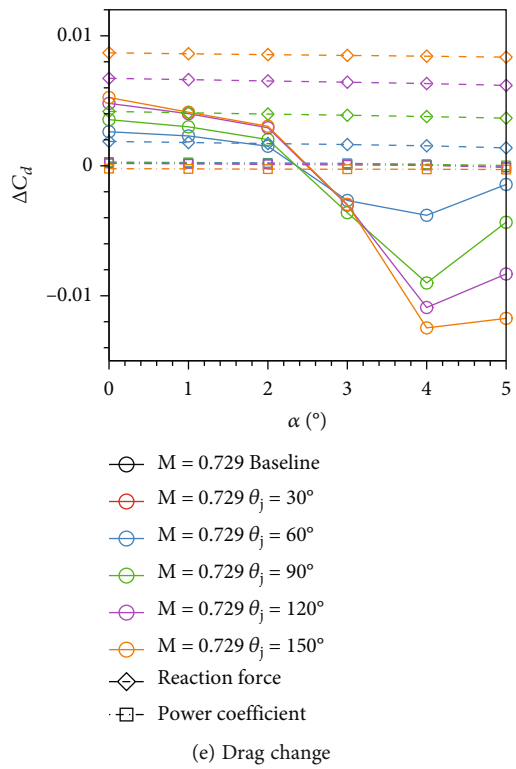

(e) Drag change

Figure 12: Transonic aerodynamic performance at $M_\infty = 0.729$ and $C_\mu = 0.005$.

3. Results

3.1. Grid Sensitivity Study. A grid sensitivity study based on the RAE2822 airfoil was carried out to ensure that the overall forces are no longer sensitive to the computational grid. This study consists of a couple of transonic flow field simulations of the RAE2822 airfoil with three levels of mesh refinement: coarse, medium, and fine. The fine mesh is the same computational mesh described in Section 2.2. Each coarser grid is generated by coarsening the finer one by a factor of 1.4 along each dimension. The freestream conditions are the Mach number $M_\infty = 0.729$, the angle of attack $\alpha = 2.31°$ and the Raynolds number $\mathrm{Re}_c = 6.5 \times 10^6$. Table 1 lists grid dimensions and corresponding aerodynamic forces. The results for all three grids are relatively close, and the drag decreases slightly as the grid gets finer. This is due to the spurious drag caused by numerical viscosity decreasing with increasing spatial resolution. The drag as a function of the grid factor is plotted in Figure 7. This plot demonstrates that we are in the asymptotic third-order convergence area because the three grid solutions and the Richardson extrapolated result are almost colinear.

3.2. Subsonic Flowfields. All five jet configurations described in Section 2.1.1 are tested in the subsonic flow. The freestream Mach number is set to $M_\infty = 0.2$, and the chord-based Reynolds number is $\mathrm{Re}_c = 6.5 \times 10^6$. The angle of attack α varies from 0° to 12°. The flowfields around these jet configurations and a baseline configuration without jets were simulated by solving the Reynolds-averaged Navier-Stokes equations.

Figure 8 shows the comparison of the aerodynamic coefficients at different jet angles. It can be seen that all of the jets can produce approximately linear lift changes up to $\alpha = 10°$. As the jet tilts from downstream ($\theta_j = 30°$) to upstream ($\theta_j = 150°$), the lift continues to reduce. On the other hand, the upstream jet increases the drag since the direction of the reaction force changes as the direction of the jet changes. As shown in Figure 8(c), the jets produce a head-up pitching moment similar to that caused by a flap deflecting upwards, but the blowing downstream ($\theta_j = 30°$) causes a nose-down pitching moment. Figures 8(d) an(d) 8(e) show the change in lift and drag, as well as the contributions of reaction forces and power consumption. Reaction forces contribute a negligible amount to the total lift reduction but are the dominant factor in drag penalties. As the jet is deflected upstream, the increase in horizontal reaction force causes an increase in drag. Nevertheless, the total drag penalty is significantly less than the increase in reaction force, indicating a decrease in aerodynamic drag as the θ_j increase. The power consumption is a small value relative to the drag penalty and decreases further as θ_j increases. This indicates that little or no additional power consumption is required to maintain the jet system. This indicates that the major control power consumption of the entire system is in the additional drag caused by the change of jet momentum.

The lift change, trimming efficiency, and power efficiency of each jet direction are compared in Figure 9. The

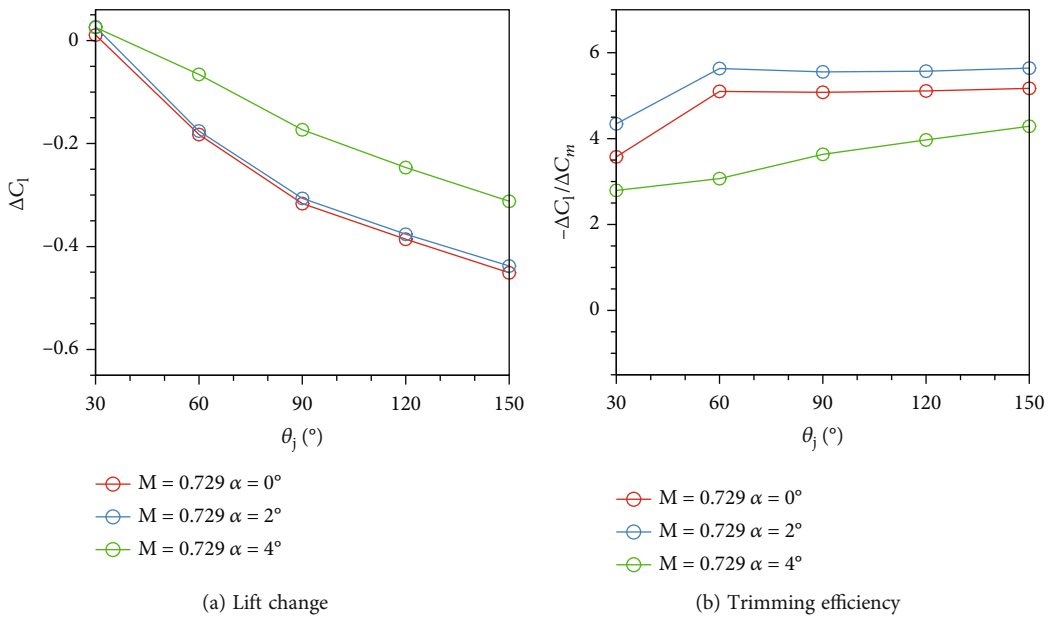

(a) Lift change (b) Trimming efficiency

Figure 13: Transonic control efficiencies of difference jets at $M_\infty = 0.729$, $\alpha = 3°$, and $C_\mu = 0.005$.

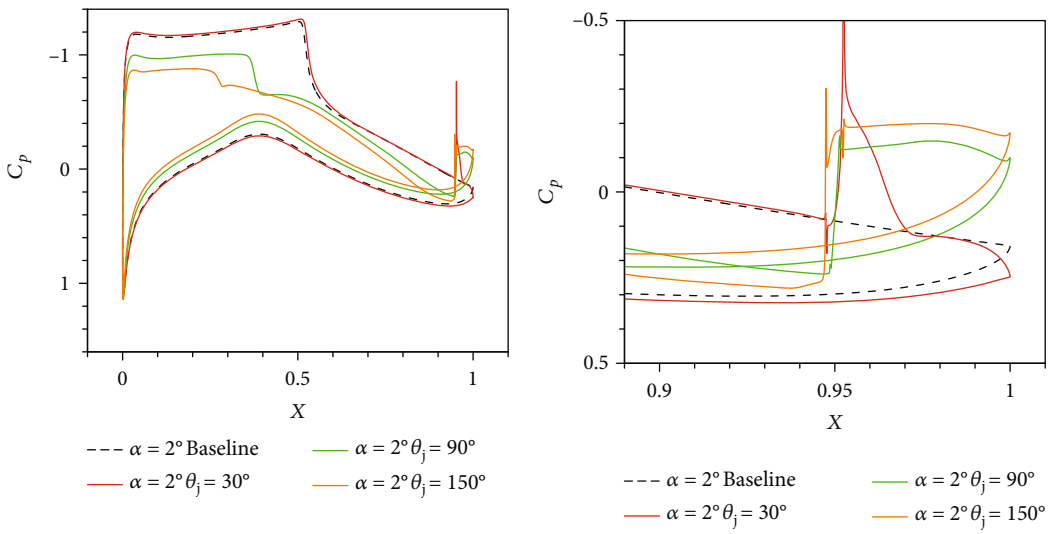

(a) Pressure distribution (b) Zoomed-in view of trailing edge

Figure 14: Pressure coefficient distributions around airfoil at $M_\infty = 0.729$, $\alpha = 3°$, and $C_\mu = 0.005$.

change in each coefficient is defined as $\Delta C_* = C_* - C_*^{(\text{baseline})}$, where $*$ can be one of l, d, and m, and $C_*^{(\text{baseline})}$ means the result of baseline airfoil under the same flow condition. The figures show that increasing the jet angle can increase the quantity of load reduction. The trimming efficiency, i.e., the lift reduction produced for the same pitching moment increase, is plotted in Figure 9(b). The trimming efficiencies for all effective jets ($\theta_j \geq 60°$) are around 5 and fall between the flap and the Conda jet result from Kahlil et al. [20]. In terms of power efficiency shown in Figure 9(c), the normal jets show a significant improvement over the downstream jets, while the upstream jets show only a minor improvement over the normal jets. These trends are consistent across the range of angles of attack from 0 to 8°.

Spence [19] has deduced that lift is linearly related to the jet angle and the angle of attack based on thin-wing potential flow theory:

$$C_l = 4\pi A_0 \tau + 2\pi(1 + 2B_0)\alpha, \tag{7}$$

$$4\pi A_0 = 3.54C_\mu^{1/2} + 0.325C_\mu + 0.156C_\mu^{3/2}, \tag{8}$$

$$4\pi B_0 = 1.152C_\mu^{1/2} + 0.106C_\mu + 0.051C_\mu^{3/2}, \tag{9}$$

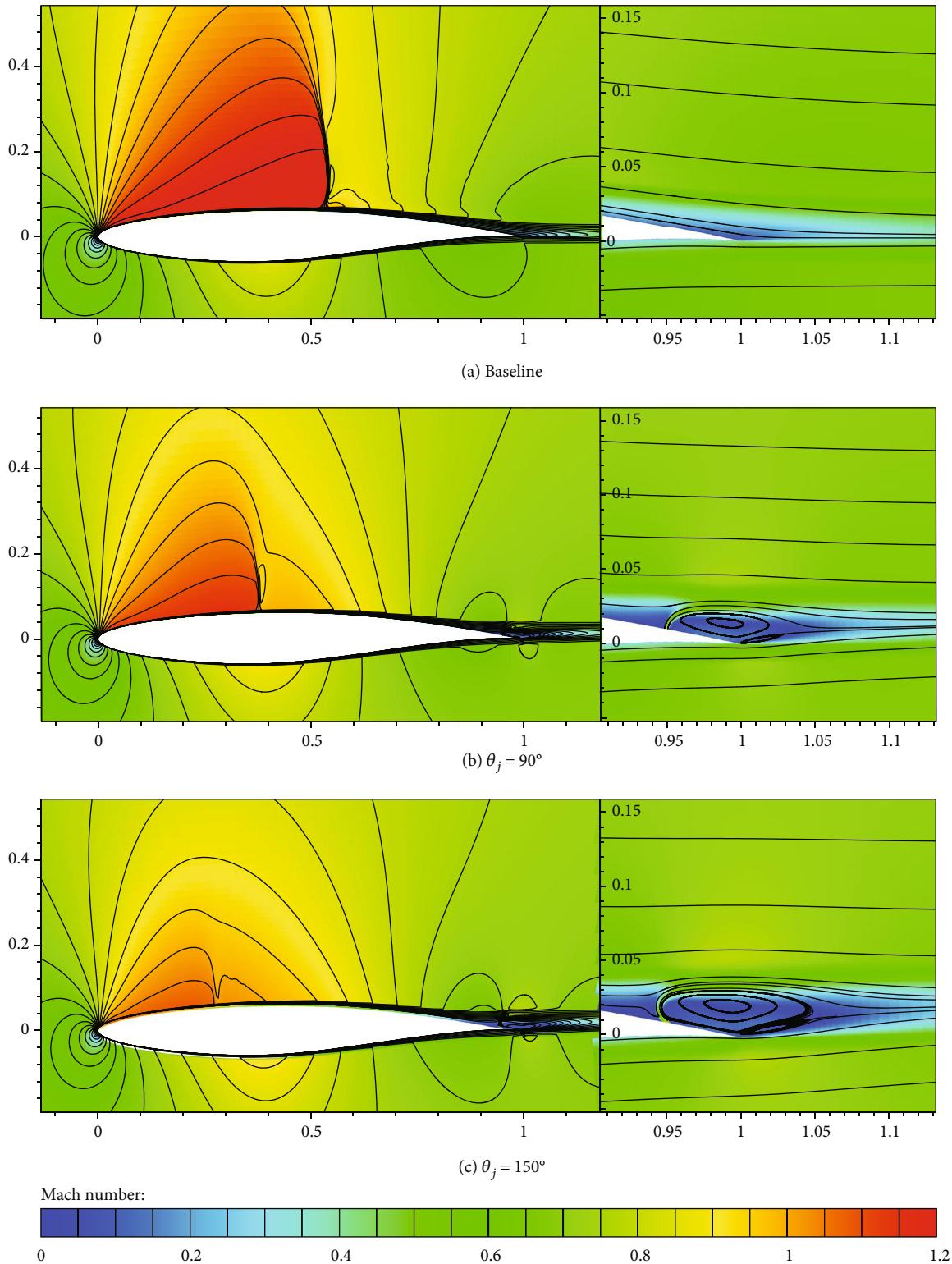

Figure 15: Mach number contours around the RAE2822 airfoil at $M_\infty = 0.729$, $\alpha = 3°$, and $C_\mu = 0.005$.

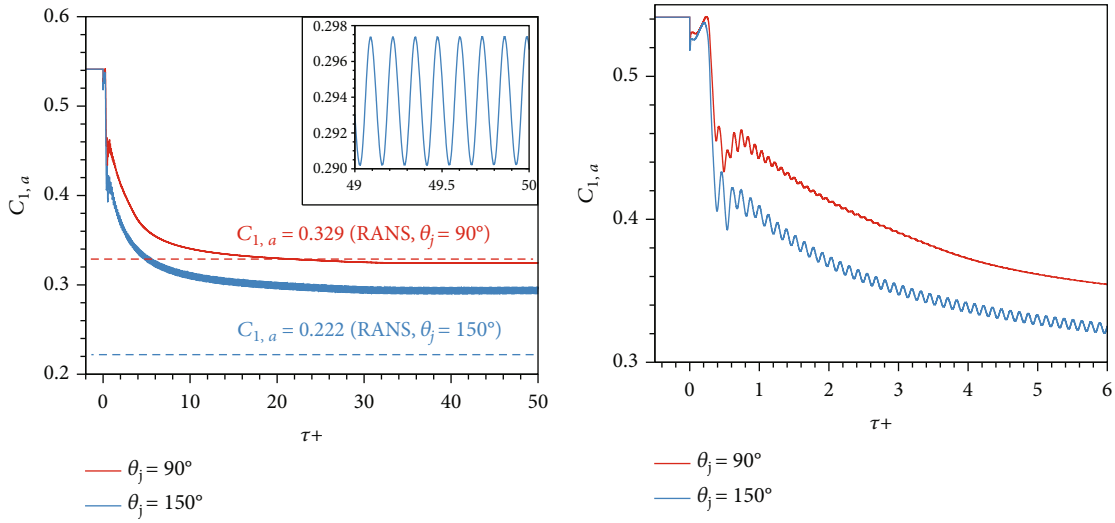

(a) Lift response

(b) Zoomed-in view

FIGURE 16: Lift responses after jet activation at $M_\infty = 0.2$, $\alpha = 3°$, and $C_\mu = 0.005$.

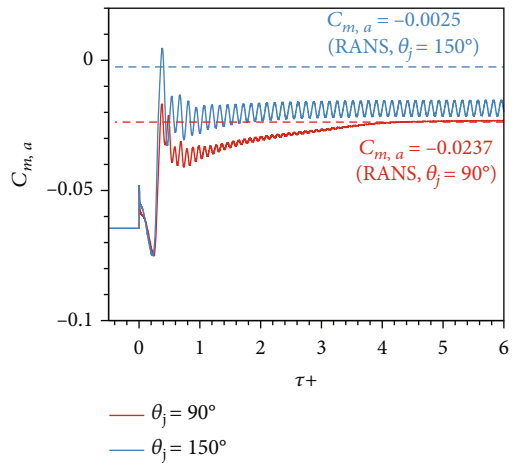

FIGURE 17: Pitching moment response after jet activation at $M_\infty = 0.2$, $\alpha = 3°$, and $C_\mu = 0.005$.

where τ is the jet deflection angle defined by Spence [19], which is opposite to the definition of θ_j, A_0, and B_0 are constants determined by the jet momentum. Obviously, the lift coefficient obtained from Equation (7) is a linear combination of θ_j and α. The derivatives of C_l with respect to θ_j and α calculated from Equations (8) and (9) are plotted as dashed triangles in Figures 9(a) and 8(d), respectively. The plots show that $dC_l/d\alpha$ redicts well, while prediciton of $dC_l/d\theta_j$ only meets at small θ_js.

Figure 10 shows the pressure coefficient distributions around the airfoil at $M_\infty = 0.2$, $\alpha = 4°$, and $C_\mu = 0.005$, and the corresponding Mach number contours and streamlines are shown in Figure 11. It can be seen that the injected jet blows the boundary layer away from the surface to form a separation zone, resulting in a pressure increase before the jet and a pressure drop after the jet. The pressure difference between the two sides also causes a deflection of the jet flow downstream. As shown in Figure 11(b), the $\theta_j = 30°$ jet causes a tiny separation bubble but then reattaches to the suction surface, so it only affects the pressure distribution in the vicinity of the jet. The recirculation zone induced by the other jets touches the trailing edge and causes a flow acceleration on the pressure side. As the jet tilts upstream, the recirculation zone grows in size, resulting in a rising blocking effect, with increased pressure on the suction surface and decreased pressure on the pressure surface.

3.3. Transonic Flowfields. This section discusses lift reduction by using microjets in the transonic flows. The transonic flows around the airfoils are more complicated due to normal shock waves on the upper surfaces. The location and strength of the shock waves have a significant influence on the airfoil lift. The transonic free-stream Mach number is $M_\infty = 0.729$, and the chord-based Reynolds number is $Re_c = 6.5 \times 10^6$.

The aerodynamic coefficients and control efficiency of different jet configurations are compared in Figures 12 and 13. The $\theta_j = 30°$ jet continues to exhibit the opposite effect, whereas all other jets can generate an almost constant lift reduction until $\alpha = 3°$. As seen in Figure 13(a), the jet with $\theta_j = 150°$ reduces as high as 42% more lift than that of the normal jet at zero angles of attack. At higher angles of attack, the lift on the baseline reaches a maximum due to shock-induced flow separations. This phenomenon is well known in the design of transonic aircraft [32]. The presence of the jet stream delays the appearance of shock-induced separation. This can be explained by the fact that the shock wave intensity also decreases as the pressure side velocity decreases, as shown in Figure 14. The additional high pressure caused by the changes in shock waves significantly reduces the airfoil lift. It can be seen that the pressure distributions near the trailing edge are similar to those in the subsonic flows, indicating a similar decamber effect caused by the trailing edge jets. Note that a reduction in the shock strength also leads to a reduction in drag, as shown in Figure 12(b). This indicates

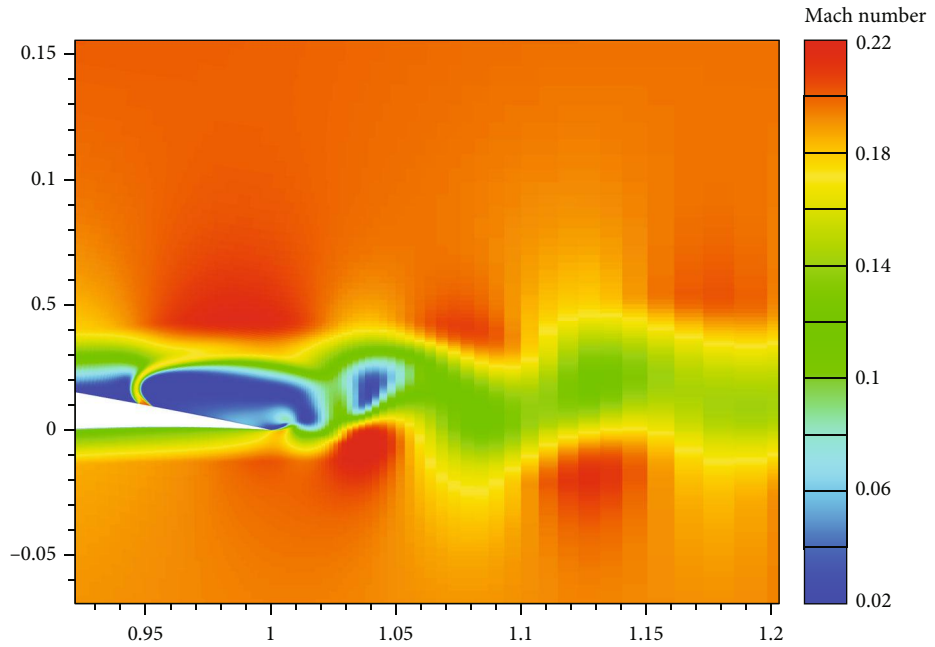

Figure 18: Flowfield in the vicinity of upstream at $\tau + = 50$, $M_\infty = 0.2$, $\alpha = 3^\circ$, and $C_\mu = 0.005$.

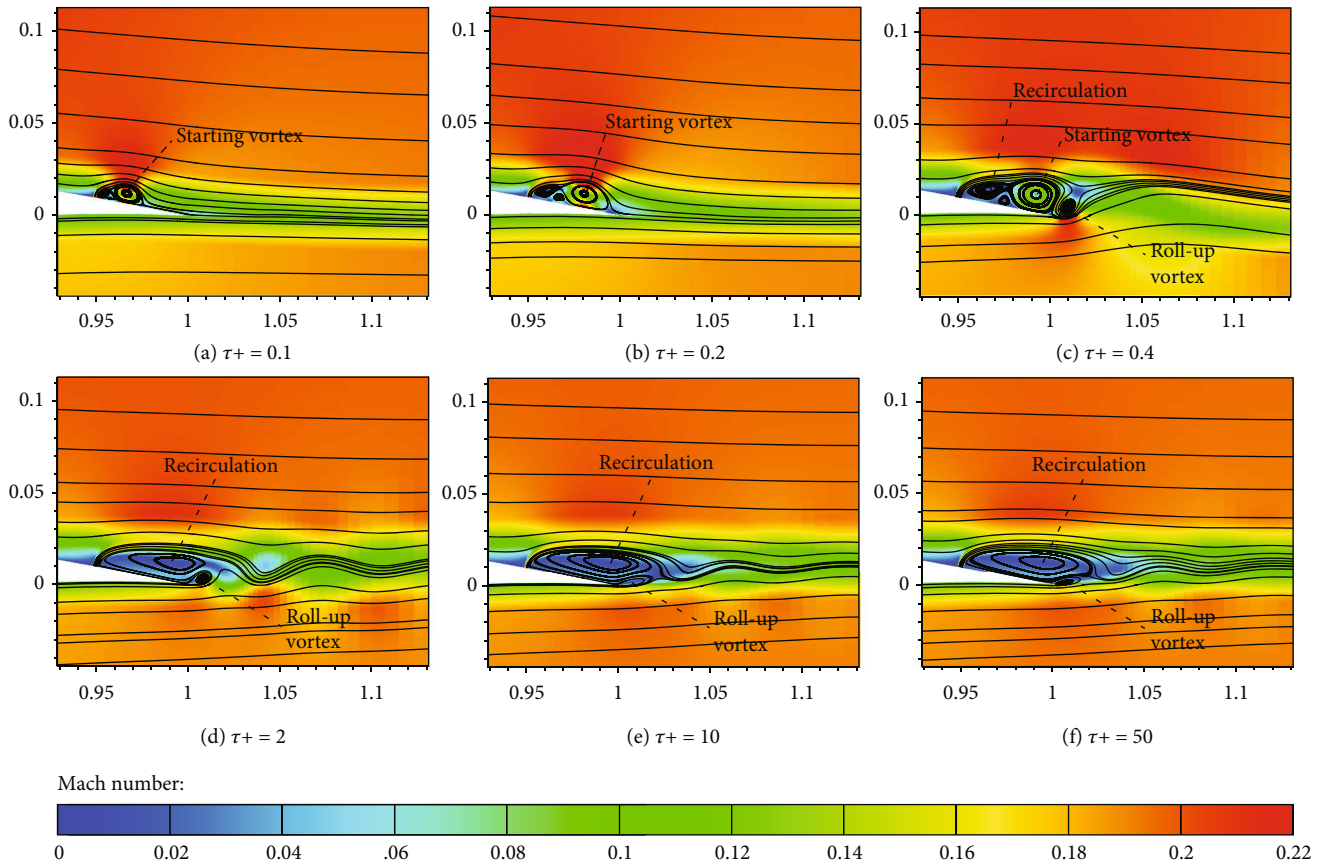

Figure 19: Flowfields in jet vicinities at $M_\infty = 0.2$, $\alpha = 3^\circ$, and $C_\mu = 0.005$

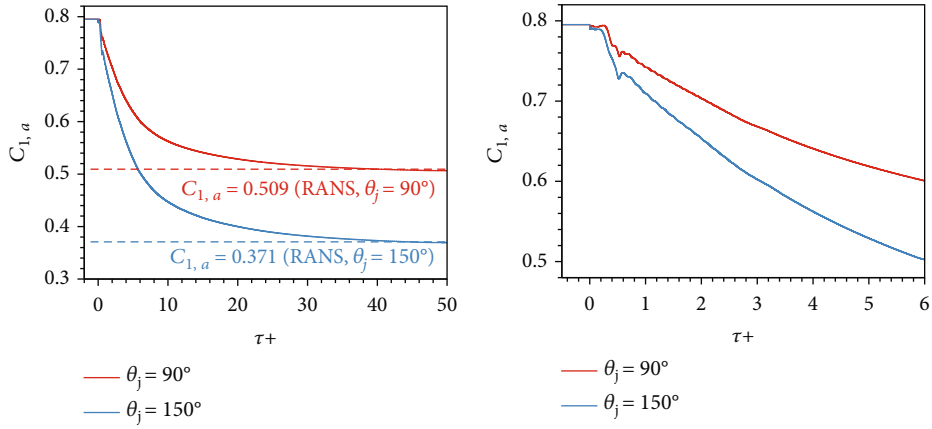

(a) Lift response (b) Zoomed-in view

Figure 20: Lift response after jet activation at $M_\infty = 0.729$, $\alpha = 3^\circ$, and $C_\mu = 0.005$.

that the microjets can decrease the total energy consumption while mitigating lift augmentation. Figure 12(e) shows that the reaction force is still an essential component of drag penalty and that any jet with $\theta_j \geq 90^\circ$ reduces aerodynamic drag. When the angle of attack is above 2 degrees, the wave drag of the baseline airfoil increases abruptly, while the jet effectively reduces the shock strength and the total drag. A head-up moment is still observed by the $\theta_j \geq 60^\circ$ jets, and their trimming efficiencies are compared in Figure 13(b). The value of $-\Delta C_l/\Delta C_m$ stays constant around 5 for $\alpha = 0^\circ$ and $\alpha = 2^\circ$ cases. However, at an angle of attack of $\alpha = 4^\circ$, the trimming efficiency decreases and the upstream jets become more efficient than the normal jet.

The Mach number contours and streamlines around the airfoil at $\alpha = 3^\circ$ are shown in Figure 15 for each jet. Except that there are supersonic flows over the upper surface, the flows near the trailing edge are very similar to those in the subsonic flows. Therefore, the same explanation can be made in the transonic flows in terms of the lift reduction caused by the blocking effect of separation bubble. In summary, there are two flow mechanisms associated with the lift reduction in transonic flows. One is the same as that in subsonic flows, and the other one is related to the changes in the position and strength of the shock waves. As observed in this study, both flow mechanisms are equally important in aerodynamic load reduction at transonic speeds.

3.4. Transient Processes of Jet Deployment. The previous RANS results already indicate that the upstream jets are more effective than the normal jets. However, Figure 11 shows a pair of vortices at the trailing edge, suggesting the presence of unsteady vortex shedding phenomena. On the other hand, in transonic flow, shock movement is another key issue that affects control effectiveness. Transient simulations were therefore carried out to test the unsteady processes in the load control process.

The deployment processes of the normal jet ($\theta_j = 90^\circ$) and the upstream jet ($\theta_j = 150^\circ$) are compared in both subsonic ($M_\infty = 0.2$) and transonic ($M_\infty = 0.729$) flows. The implicit second-order dual time-stepping is adopted for time

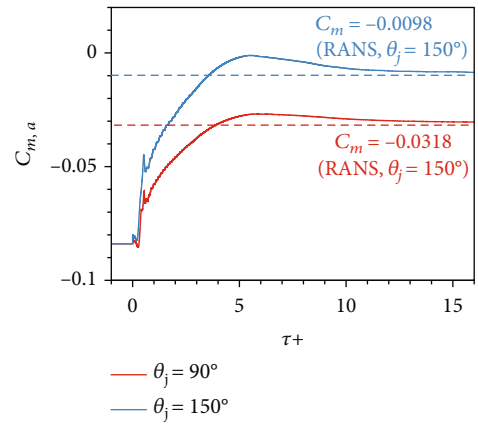

Figure 21: Pitching moment response after jet activation at $M_\infty = 0.729$, $\alpha = 3^\circ$, and $C_\mu = 0.005$.

marching starting from a converged baseline flow. The global time step is $\tau = 2 \times 10^{-4}$, where $\tau = tU_\infty/c$ is the convective time unit and t is the physical time.

The lift and pitching moment history of subsonic cases, as well as the RANS results, are plotted in Figures 16 and 17. The freestream Mach number is $M_\infty = 0.2$, the angle of attack is $\alpha = 3^\circ$, and the Reynolds number is $\mathrm{Re}_c = 6.5 \times 10^3$. The horizontal axis is the convective time unit after the jet activation at $\tau + = 0$. First of all, oscillations in lift and pitching moment are observed in upstream jet results. This is due to the vortex shedding phenomenon as shown in Figure 18. Also, the lift and moment cannot converge to the RANS results due to the inability to form a stable recirculation region. Observing the responses of the normal jet and in combination with the transient flowfield shown in Figure 19, it can be found that the aerodynamic response can be divided into three stages:

(i) *Time lag* is observed before $\tau + = 0.2$. At the moment of jet activation, the flow field near the jet is altered and a starting vortex is induced. This resulted in a lift and moment fluctuation, but the

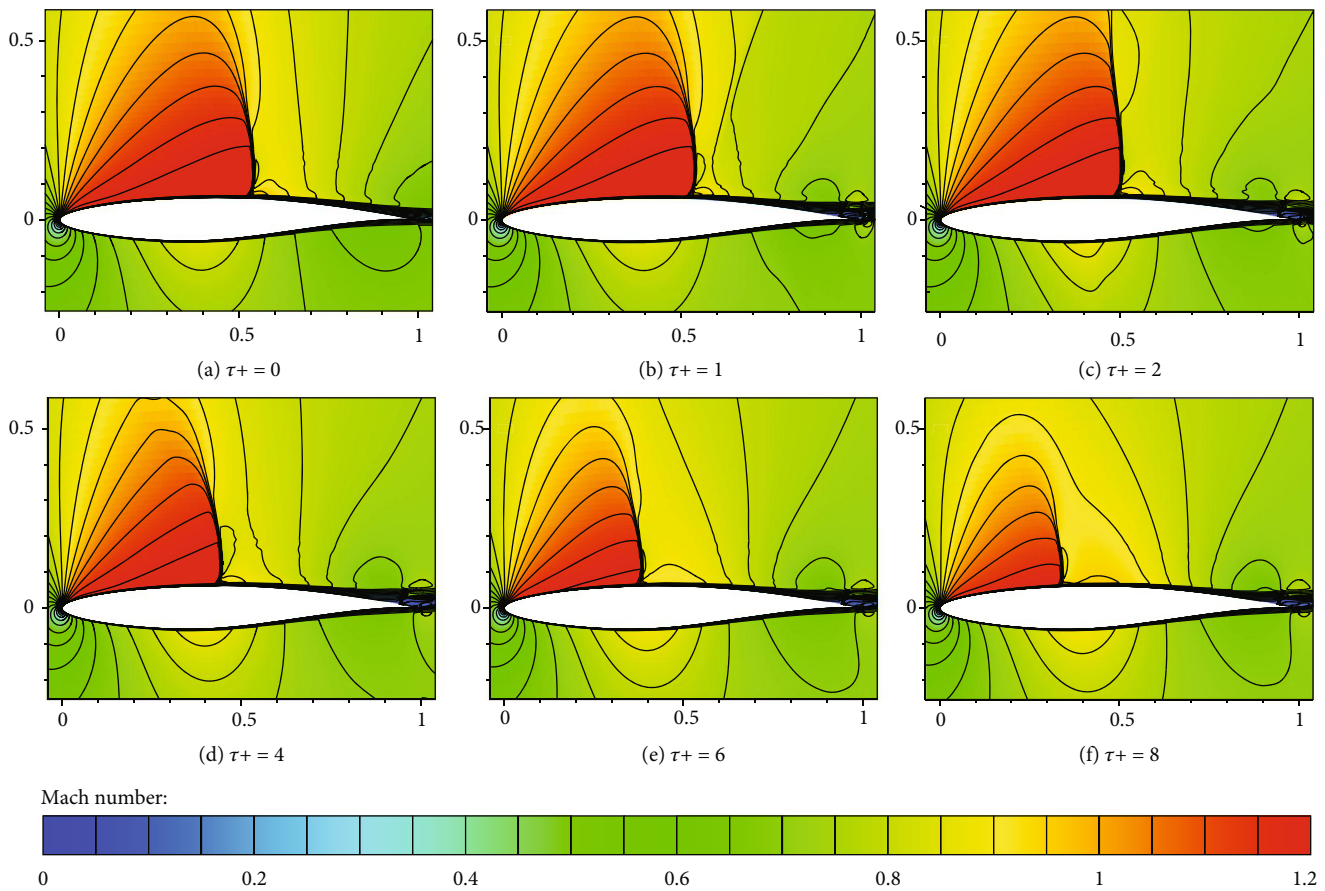

Figure 22: Transient flowfields around RAE2822 airfoil with upstream jet at $M_\infty = 0.729$, $\alpha = 3^\circ$, $\theta_j = 150^\circ$, and $C_\mu = 0.005$.

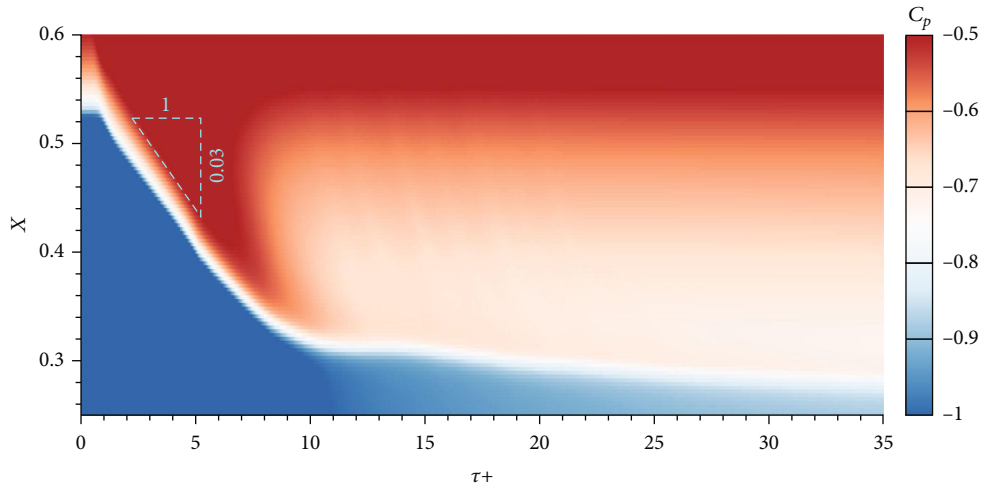

Figure 23: Pressure history on suction surface at $M_\infty = 0.729$, $\alpha = 3^\circ$, $\theta_j = 150^\circ$, and $C_\mu = 0.005$.

trailing edge was not affected. As the initiating vortex moves downstream, the reflux zone begins to grow gradually. The recirculation zone grows gradually as the starting vortex moves downstream

(ii) *A vortex rolls up* once the low pressure of starting vortex reaches the trailing edge. This results in a reduction in circulation and an upward deflection of the wake during $\tau +$ between 0.2 and 0.4. The change in the trailing edge flowfield also results in a rapidly increasing head-up moment

(iii) *Rebalancing of flowfield* is the next stage after the starting vortex leaves the airfoil. As the recirculation

zone gradually stabilizes, the roll-up vortex shrinks and the amplitude of lift and pitch moment decreases. The lift force reaches a steady state around $\tau+ = 30$. And the pitching moment is stabilized at around $\tau+ = 5$. Although there are still vortices rolling up and shedding from the airfoil, the amplitude of lift oscillation is only 1.7×10^{-4}

Figures 20 and 21 show the lift and pitching moment response in transonic flow at a Mach number $M_\infty = 0.729$, an angle of attack of $\alpha = 3°$, and a Reynolds number $\mathrm{Re}_c = 6.5 \times 10^6$. The lift of both the normal jet and the upstream jet converged to RANS results at about $\tau+ = 40$ without any obvious oscillation. While the pitching moments converged close to the RANS results at $\tau+ = 10$ with an overshoot at $\tau+ = 3.6$. The lift response process can still be divided into three stages, but the percentage of lift reduction induced by the starting vortex is significantly reduced. During the phase of flowfield rebalancing, the movement and weakening of the shock provide an additional lift reduction.

Figure 22 shows the transient flowfields around the airfoil equipped with the upstream jet. At $\tau+ = 1$, the pressure increase caused by flow obstruction at the trailing edge has just touched the shock, but the shock position has not yet begun to change noticeably. At $\tau+ = 2$, the high pressure behind the shock wave drives it forward, while the flow field in front of the shock wave remains almost unaltered. Simultaneously, the lower surface flow acceleration can be observed to have spread from the trailing edge to the middle of the airfoil. After $\tau+ = 4$, when the lower surface acceleration zone reaches the leading edge, the strength of shock begins to decrease as it continues to move forward.

Figure 23 displays the time-dependent variation of the upper surface pressure coefficient. The graph reveals that the shock travels with an almost constant velocity of $dx/d\tau = 0.03$ between $\tau+ = 1$ and 5, corresponding to the increase of pitching moment in Figure 21. Between $\tau+ = 5$ and 10, the Mach number before the shock and the pressure after the shock decrease gradually as the shock travel speed begins to decelerate.

4. Conclusions

This paper reports a numerical investigation of the influence of jet-blowing direction on the effectiveness of aerodynamic load control at both subsonic and transonic speeds.

It can be concluded that both upstream and normal microjets can produce effective lift reduction at a range of angles of attack, while the upstream jet is the most effective in controlling the load at the same condition. It can be explained by the fact that the jet blowing upstream creates a larger flow separation region than that of the normal jet, further increasing the pressure on the suction surface.

Moreover, for transonic flows, the lift reduction is amplified by the changes in the normal shock wave location and strength on the upper surface. The flow separation bubble induced by the jets moves the shock wave forward while reducing the shock strength, significantly increasing the lift reduction.

In terms of power consumption, the normal jets and the upstream jets are comparable in efficiency at low speeds. In transonic flows, the upstream jets not only reduce the lift but also mitigate the drag increase caused by the reinforced normal shock at $\alpha \geq 3°$, resulting in a reduction of the overall power consumption.

Unfortunately, as shown by the unsteady results, the upstream jet induces strong vortex shedding, which diminishes the control effect and generates severe lift and pitch moment oscillations. Vortex shedding is suppressed and obvious oscillations are not observed in transonic flow.

There are three stages during the jet deployment process: time lag, vortex rolling-up, and rebalancing. In subsonic flows, the starting vortex rapidly modifies the lift and pitch moment once reaching the trailing edge. In transonic flow, however, the rebalancing stage contributes to a greater drop in lift due to the additional shock movement and weakening effect.

In conclusion, the upstream jet is more suited for transonic flows due to its higher load control authority and ability to delay drag divergence caused by the increasing angle of attack. Meanwhile, the normal jet is better for low-speed flows because of its more stable recirculation zone and load response.

Abbreviations

C_μ: Jet momentum coefficient
$\dot{m}$: Mass flow rate
ρ_∞: Freestream density
U_∞: Freestream velocity magnitude
M_∞: Freestream Mach number
c: Airfoil chord
ρ_j: Jet air density
U_j: Jet flow velocity magnitude
x_j: Chordwise location of jet center
h_j: Jet slit width
θ_j: Jet direction angle
w_j: Jet exit width
P_{jet}: Power consumption of pump
c_p: Specific heat at constant pressure
η: Pump efficiency
T_{00}, T_{01}: Total temperature before and after pump
T_{00}, T_{01}: Total pressure before and after pump
Γ: Total pressure ratio of pump
γ: Specific heat ratio
C_{power}: Power coefficient of pump
Re_c: Chord-based Reynolds number
$\vec{r}$: Reaction force of jet flow
$\vec{u}_j$: Jet velocity vector
$\vec{u}_\infty$: Freestream velocity vector
C_l: Lift coefficient
C_d: Drag coefficient
C_m: Pitching moment coefficient
$\square_a$: Surface integrated forces and moments
$\square_r$: Contribution of reaction force

τ: Convective time unit.

Data Availability

The computational data used to support the findings of this study are available from the corresponding author upon request.

Conflicts of Interest

The authors declare that they have no known competing financial interests or personal relationships that could have appeared to influence the work reported in this paper.

Acknowledgments

This research was funded by the projects supported by the National Natural Science Foundation of China (grant numbers 11672132, 12032011, and 11502112) and a project funded by the Priority Academic Program Development of Jiangsu Higher Education Institutions.

References

[1] F. M. Hoblit, "Gust Loads Fundamentals," in *Gust Loads on Aircraft: Concepts and Applications*, pp. 1–6, American Institute of Aeronautics and Astronautics, Washington, DC, USA, 1988.

[2] V. Handojo, *Contribution to load alleviation in aircraft predesign and its influence on structural mass and fatigue*, Technische Universitat, Berlin, Berlin, 2020, https://depositonce.tu-berlin.de/handle/11303/12111.

[3] T. E. Disney, "C-5a active load alleviation system," *Journal of Spacecraft and Rockets*, vol. 14, no. 2, pp. 81–86, 1977.

[4] J. F. Johnston, *Accelerated development and flight evaluation of active controls concepts for subsonic transport aircraft. Volume 1: load alleviation/extended span development and flight tests*, Technical Report NASA-CR-159097, NASA, 1979.

[5] S. Biringen, "Active control of transition by periodic suction-blowing," *Physics of Fluids*, vol. 27, no. 6, p. 1345, 1984.

[6] J. P. Johnston and M. Nishi, "Vortex generator jets - means for flow separation control," *AIAA Journal*, vol. 28, no. 6, pp. 989–994, 1990.

[7] R. H. Liebeck, "Design of subsonic airfoils for high lift," *Journal of Aircraft*, vol. 15, no. 9, pp. 547–561, 1978.

[8] R. Radespiel, M. Burnazzi, M. Casper, and P. Scholz, "Active flow control for high lift with steady blowing," *Aeronautical Journal*, vol. 120, no. 1223, pp. 171–200, 2016.

[9] D. T. Yen Nakafuji, C. P. van Dam, R. L. Smith, and S. D. Collins, "Active load control for airfoils using microtabs," *Journal of Solar Energy Engineering*, vol. 123, 2001.

[10] M. Blaylock, R. Chow, and C. P. van Dam, "Comparison of microjets with microtabs for active aerodynamic load control," in *5th Flow Control Conference*, American Institute of Aeronautics and Astronautics, 2010.

[11] N. H. Al-Battal, D. J. Cleaver, and I. Gursul, "Lift reduction by counter flowing wall jets," *Aerospace Science and Technology*, vol. 78, pp. 682–695, 2018.

[12] Y. Li and N. Qin, "Airfoil gust load alleviation by circulation control," *Aerospace Science and Technology*, vol. 98, article 105622, 2020.

[13] D. Heathcote, D. Cleaver, and I. Gursul, "Frequency response of aerodynamic load control through mini-tabs," in *55th AIAA Aerospace Sciences Meeting*, American Institute of Aeronautics and Astronautics, 2017.

[14] C. Chen, R. Seele, and I. Wygnanski, "Flow control on a thick airfoil using suction compared to blowing," *AIAA Journal*, vol. 51, no. 6, pp. 1462–1472, 2013.

[15] Z. Wang and I. Gursul, "Lift enhancement of a flat-plate airfoil by steady suction," *AIAA Journal*, vol. 55, no. 4, pp. 1355–1372, 2017.

[16] M. V. Cook, A. Buonanno, and S. D. Erbsloh, "A circulation control actuator for flapless flight control," *Aeronautical Journal*, vol. 112, no. 1134, pp. 483–489, 2008.

[17] D. A. Wetzel, J. Griffin, and L. N. Cattafesta, "Experiments on an elliptic circulation control aerofoil," *Journal of Fluid Mechanics*, vol. 730, pp. 99–144, 2013.

[18] M. G. Alexander, S. G. Anders, S. K. Johnson, J. P. Florance, and D. F. Keller, "Trailing edge blowing on a two-dimensional six-percent thick elliptical circulation control airfoil up to transonic conditions," Technical Report NASA/TM-2005-213545, NASA, 2005.

[19] D. A. Spence, "The lift coefficient of a thin, jet-flapped wing," *Proceedings of the Royal Society of London. Series A. Mathematical and Physical Sciences*, vol. 238, no. 1212, pp. 46–68, 1956.

[20] K. Khalil, S. Asaro, and A. Bauknecht, "Active flow control devices for wing load alleviation," *Journal of Aircraft*, vol. 59, no. 2, pp. 458–473, 2022.

[21] N. H. Al-Battal, D. J. Cleaver, and I. Gursul, "Unsteady actuation of counter-flowing wall jets for gust load attenuation," *Aerospace Science and Technology*, vol. 89, pp. 175–191, 2019.

[22] Y. Li and N. Qin, "Gust load alleviation by normal microjet," *Aerospace Science and Technology*, vol. 117, article 106919, 2021.

[23] A. Lefebvre, B. Dano, W. B. Bartow, M. Difronzo, and G. C. Zha, "Performance and energy expenditure of coflow jet airfoil with variation of Mach number," *Journal of Aircraft*, vol. 53, no. 6, pp. 1757–1767, 2016.

[24] D. W. Kinsey and T. J. Barth, *Description of a hyperbolic grid generating procedure for arbitrary two-dimensional bodies*, AIR FORCE WRIGHT AERONAUTICAL LABS WRIGHT-PATTERSON AFB OH, 1984.

[25] S. L. Krist, R. T. Biedron, and C. L. Rumsey, *Cfl3d User's Manual (Version 5.0)*, The NASA Langley Research Center, Hampton, VA, 1998.

[26] B. Van Leer, "Upwind-difference methods for aerodynamic problems governed by the Euler equations," in *Large-Scale Computations in Fluid Mechanics, Part 2*, B. E. Engquist, S. Osher, and R. C. J. Somerville, Eds., pp. 327–336, American Mathematical Society, 1985.

[27] P. L. Roe, "Approximate Riemann solvers, parameter vectors, and difference schemes," *Journal of Computational Physics*, vol. 43, no. 2, pp. 357–372, 1981.

[28] F. R. Menter, M. Kuntz, and R. Langtry, "Ten years of industrial experience with the SST turbulence model," *Turbulence, heat and mass transfer*, vol. 4, no. 1, pp. 625–632, 2003.

[29] P. E. Smirnov and F. R. Menter, "Sensitization of the SST turbulence model to rotation and curvature by applying the Spalart–Shur correction term," *Journal of turboma chinery*, vol. 131, no. 4, 2009.

[30] M. Blaylock, R. Chow, A. Cooperman, and C. P. van Dam, "Comparison of pneumatic jets and tabs for active aerodynamic load control," *Wind Energy*, vol. 17, pp. 1365–1384, 2013.

[31] H. de Vries, C. Boeije, I. Cleine et al., "Fluidic load control for wind turbine blades," in *47th AIAA Aerospace Sciences Meeting Including the New Horizons Forum and Aerospace Exposition*, American Institute of Aeronautics and Astronautics, 2009.

[32] E. Obert, *Aerodynamic Design of Transport Aircraft*, Ios Press ; Delft University of Technology, Faculty of Aerospace Engineering, Section Design of Aircraft and Rotorcraft, Amsterdam, NY, 2009.